ELSEVIER

Journal of Volcanology and Geothermal Research 103 (2000) 439–462

Journal of volcanology and geothermal research

www.elsevier.nl/locate/jvolgeores

A double seismic antenna experiment at teide Volcano: existence of local seismicity and lack of evidences of Volcanic tremor

J. Almendros[a], J.M. Ibáñez[a,b,*], G. Alguacil[a,b], J. Morales[a,b], E. Del Pezzo[c], M. La Rocca[d], R. Ortiz[e], V. Araña[e], M.J. Blanco[f]

[a]*Instituto Andaluz de Geofísica, Universidad de Granada, Campus de Cartuja s/n, 18071 Granada, Spain*
[b]*Departamento de Física Teórica y del Cosmos, Universidad de Granada, 18071 Granada, Spain*
[c]*Osservatorio Vesuviano, Centro di Sorvegianza, Via A. Manzoni 249, 80123 Naples, Italy*
[d]*Dipartimento di Fisica, Universitá di Salerno, Baronissi, Salerno, Italy*
[e]*Departamento de Volcanología, Museo Nacional de Ciencias Naturales, CSIC, C/José Gutiérrez Abascal, no. 2, 28006 Madrid, Spain*
[f]*Centro Regional de Canarias del Instituto Geográfico Nacional, Santa Cruz de Tenerife, Spain*

Received 8 February 1999; revised 5 November 1999; accepted 29 November 1999

Abstract

Data analyzed in the present work correspond to a 40 days field experiment carried out in Teide Volcano (Canary Islands, Spain) with two short-period small-aperture dense seismic antennas in 1994. The objective of this experiment was to detect, analyze and locate the local seismicity. We analyzed also the background seismic noise to investigate the possible presence of volcanic tremor. From a set of 76 events, we selected 21 of them in base of their good signal-to-noise ratio and their possibility to locate their seismic source by using the seismic antennas. A visual classification based on the S–P time and seismogram shape has permitted to establish three groups of events: local seismicity (S–P time between 3 and 5 s), very local earthquakes (S–P time smaller than 3 s) and artificial explosions. These earthquakes have been located by applying the Zero Lag Cross-Correlation technique and the inverse ray-tracing procedure. Those earthquakes that were recorded simultaneously by both seismic antennas were also located by intersecting both back-azimuths. The analysis of the seismicity has revealed that the amount of seismicity in Teide Volcano is moderate. This seismicity could be distributed in three main areas: inside the Caldera Edifice (below the Teide–Pico Viejo complex), in the eastern border of the Caldera Edifice and offshore of the island. At present, this activity is the only indicator of the volcano dynamics. The analysis of the back-ground seismic noise has revealed that at frequencies lower than 2 Hz, the Oceanic Load signal is predominant over other signals, even over local earthquakes with a magnitude of 2.0. Due to this, although if in the Teide area were present a weak volcanic tremor, or other volcanic signals with predominant peaks below 2 Hz, to observe them would be a very difficult task.

Keywords: Teide Volcano; seismic antennas; volcano-tectonic earthquakes; back-ground seismic noise

1. Introduction

The aim of the present paper is to analyze the results obtained from an experiment with a double seismic antenna carried out at Teide Volcano (Canary Islands, Spain) in the autumn 1994. Teide Volcano is

* Corresponding author. Fax: +34-958-160907.
E-mail addresses: alm@iag.ugr.es (J. Almendros), ibanez@iag.ugr.es (J.M. Ibáñez), alguacil@iag.ugr.es (G. Alguacil), morales@iag.ugr.es (J. Morales), delpezzo@osve.unina.it (E. Del Pezzo), larocca@axpgo.phys.unisa.it (M. La Rocca), mcnor72@pinar1.csisc.es (R. Ortiz), mblanco@ign.es (M.J. Blanco).

0377-0273/00/$ - see front matter
PII: S0377-0273(00)00236-5

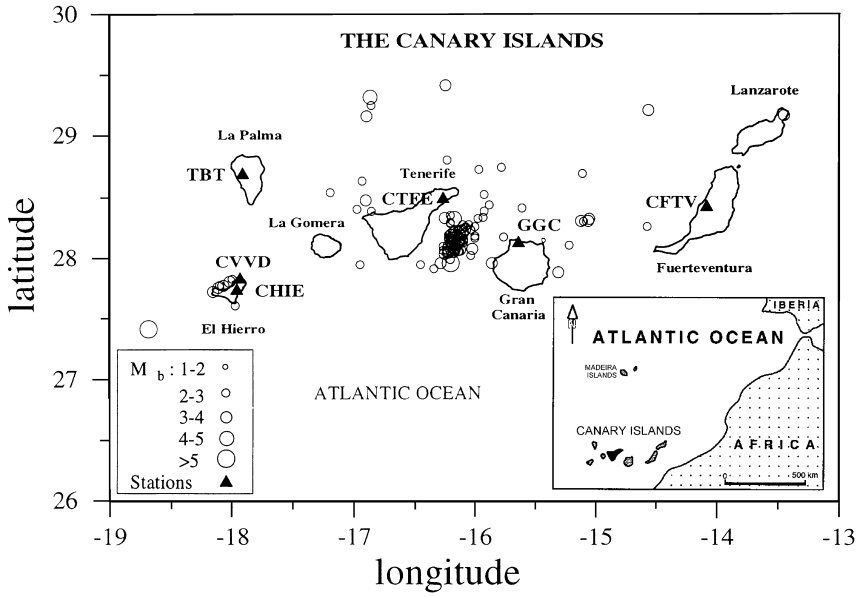

Fig. 1. Position map of Canary Island in which the seismicity of the 1991–1996 period is included. Some of the seismic stations belonging to the Spanish Seismic Network are represented by filled triangles.

the highest elevation (3718 m) of the Canary Islands archipelago. It is located at 28°18′ N and 16°36′ W, at the northwest of Africa (Fig. 1). The central area of Tenerife has been quiescent since the Chinyero eruption (1909), and the only external manifestation of volcanic activity is a fumarolic field in the top of the Teide summit. However, the Teide Volcano is potentially dangerous due to the explosive character of some of its pre-historical eruptions and the high density of population living in the neighborhood of the volcano edifice. An example of its explosive activity was the Montaña Blanca sub-plinean eruption, occurred 2020 years ago (Ablay et al., 1995a). Several geophysical studies and experiments have been carried out in Canary Island and at Teide Volcano: gravimetric and geodetic (Filmer and McNutt, 1989; Sevilla and Romero, 1991; Watts, 1994); magnetotelluric (Ortiz et al., 1986), regional seismicity and attenuation (Canas et al., 1998) and magnetic surveys (Blanco, 1997). Only a few studies about local seismic activity have been carried out (Mezcua et al., 1990; Del Pezzo et al., 1997). The regional seismic activity of the area could be considered as moderate with earthquakes with magnitude less than 5.0 (Mezcua et al., 1992), and mainly concentrated between the two major islands (Tenerife and Gran Canaria, see Fig. 1). No reported seismic activity has been directly associated with the Teide Volcano structure.

The micro-seismicity associated to a volcanic region can be monitored and studied by using a short period seismic network around the area of interest. The use of short period and small aperture seismic antennas (or seismic arrays) to study the seismicity associated with volcanic regions begin to be spread (e.g. Kilauea: Goldstein and Chouet, 1994; Masaya: Métaxian et al., 1997; Stromboli: Saccorotti, 1997; Deception Island: Alguacil et al., 1999). The seismic antennas are a more powerful tool than the ordinary seismic network when they are used, for example, to locate and track the position of the volcanic tremor source (Almendros et al., 1999); to establish the relationship among some volcanic signals (Almendros et al., 1997); to determine the nature of the wave field and local structure (Ferrazzini et al., 1991), etc. Moreover, the use of the seismic arrays permits to detect and analyze earthquakes with a very low magnitude. The array techniques permit to identify the arrival of coherent phases (P, S or other), even when the signal-to-noise ratio is unfavorable.

In the experiment carried out in Teide Volcano, two

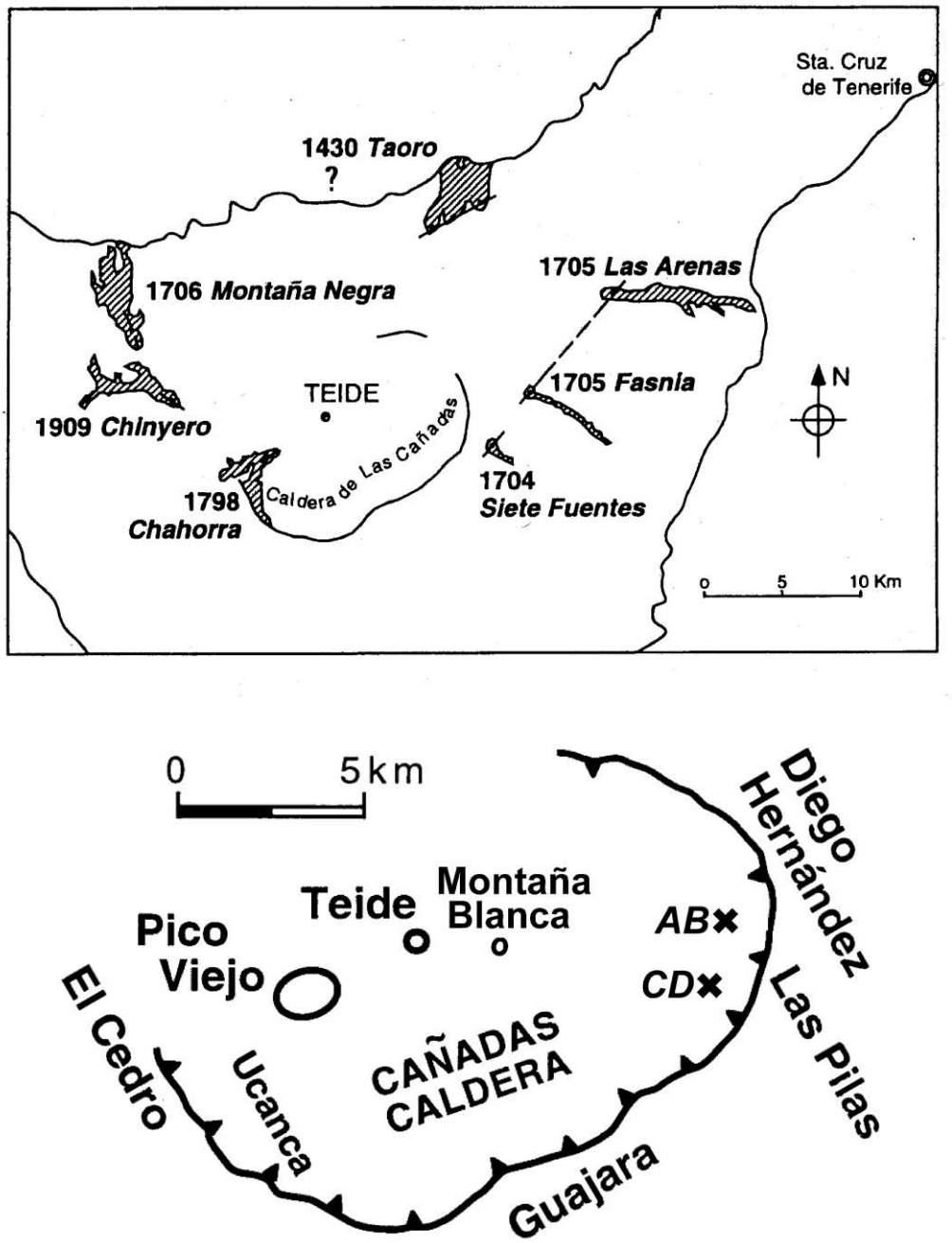

Fig. 2. (Up) Detailed map of Tenerife Island in which the main historical eruptions are represented. (Down) Detailed map of Las Cañadas Caldera showing the position of the three main structures, Teide–Pico Viejo complex and Montaña Blanca. Crosses represent the position of the seismic antennas (AB and CD) and the single stations (E and F) used in this study.

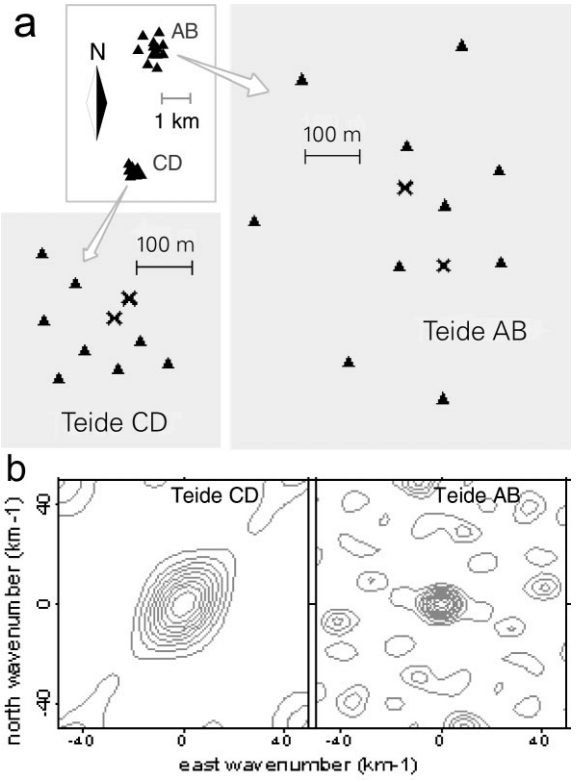

Fig. 3. (Up) Detailed map of the seismic antennas deployed in Las Cañadas Caldera. Filled triangles represent vertical seismometers and crosses show the position of the three components sensors. (Down) The array-response functions for both arrays.

short-period small-aperture seismic arrays were deployed in the Cañada de Diego Hernández, inside of the Teide–Cañadas complex (Fig. 2). Two three-component short-period (1 Hz) seismic stations were also installed on hard rock of the caldera border. We registered information for a period of 40 days since middle of September 1994. The objective of this experiment was to detect, locate and analyze the local seismic activity of the area, and to investigate the nature of the seismic noise to look for the possible presence of volcanic tremor or long period events.

2. Experiment: site and instruments

2.1. Geological setting

The oldest materials in Tenerife (between 11.6 and 3.3 Ma ago, according to Ancochea et al., 1990) constitute three basaltic shields that crop out in the NE (Anaga), NW (Teno) and S (Roque del Conde) of the island. After, two basaltic ridges were formed over volcano-tectonic axis (NE–SE and NW–SE) whose maximum eruptive activity occurred 0.8 Ma ago (Ancochea et al., 1990). The ridges converge in the central region of the island, occupied by a great stratovolcano named Edificio Cañadas. The eruptions of Edificio Cañadas began 3 Ma ago, and constitute several long-term (100–300 ka) cycles of phonolitic explosive activity, each ending with a mayor caldera collapse event (Martí et al., 1994, 1995).

The Cañadas Caldera is an elliptical depression at an altitude of approximately 2000 m, measuring 16×9 km, with a maximum depth of 600 m below the top of the caldera wall at Guajara (2717 m). The present caldera rim comprises several scalloped walls. A large spur (Roques de García) divides the caldera into two parts, the western depression being 150 m deeper than the eastern one. The caldera wall is visible 27 km along the SW, SE, E and NE sectors, being partially open in the North at El Portillo. This caldera is multicyclic collapse caldera that formed over the period 1.18–0.17 Ma (Martí et al., 1994, 1995).

The Diego Hernández and the Las Pilas formations are exposed in the eastern and northeastern sides of the caldera wall. They are the youngest formations of the Cañadas caldera system and show a more restricted distribution of materials than the older formations. A stratigraphic section of the Diego Hernández wall includes several basaltic lava flows with intercalated strombolian fallout deposits, plinian air-fall deposits, surge deposits, pumice-rich ignimbrites, lithic-rich ignimbrites and co-lag breccias. This formation has a maximum thickness of 250 m in the wall. The age of this formation range between 370 and 170 ka. The Diego Hernández formation was built up into two stages separated by a period of erosion and non-deposition. The first stage was a basalt lava. The second one, representing the main part of its sequence, occurred between 266 and 179 ka. This sequence includes several pumitic deposits and interbedded lapilli deposits and basaltic lavas, derived from the strombolian cones located at the northern margin of the Diego Hernández wall (Martí et al., 1994, 1995).

The presence of normal concentric faults, affecting

different stratigraphic levels, has been observed in the Las Cañadas caldera wall. It is significant that the existence of reverse radial faults in some sectors of the Las Cañadas, as Diego Hernández, La Angostura or Montón de Trigo (Ablay and Martí, 1995).

The last cycle of the Cañadas Edifice corresponds to the Pico Viejo–Teide (3718 m) complex. This complex begun its activity after the last collapse event, 170 ka ago. These volcanoes are located in the north of the Cañadas caldera, and partially infilled it with their products. The last explosive eruption in the Teide system took place 2020 years ago. The eruptive column reached 15 km and around 0.25 km^3 of volatile-rich magma was erupted, producing the pumitic deposit of Montaña Blanca (Ablay et al., 1995).

In historical periods, several minor eruptions have been recorded, all of them of basaltic type. The most recent eruptions were the Siete Fuentes, Fasnia, Arenas and Montaña Negra in 1704–1706, some of them near the Diego Hernández wall. Other eruption (Chahorra Volcano) occurred at the Teide southern slopes in 1789. The last eruption took place in the NW–SE ridge, near the Pico Viejo, in 1909 (see Fig. 2).

2.2. Seismic instruments

We deployed two clusters of seismometers or seismic arrays, Fig. 3. The first antenna, named array AB, was deployed in the Diego Hernández Formation, and was composed by ten vertical seismometers and two three-component sensors. Its geometry was approximately circular with a diameter of about 600 m. The second cluster, array CD, was deployed in the Las Pilas Formation and was composed of eight vertical seismometers and two three-component sensors. The geometry of this array was triangular with an aperture of about 300 m. Each seismic array was composed of two independent eight channels modules. Each module had eight seismometers with preamplifiers close to them, a 16 bits data acquisition system and a GPS time receiver. All the seismometers used in the cluster AB were Mark L15 and, in the array CD, were Mark L25, all of them with natural frequency of 4.5 Hz. Their response was electronically extended to 1 Hz. Each sensor has a preamplifier that permits to send the signal via cable to the data logger. The data acquisition system is composed of: (a) an eight channel anti-alias Butterworth multipole filter at 48 Hz; (b) a multiplexer that samples the eight channels every 5 ms; (c) a 16 bit A/D converter. The internal clock is synchronized by GPS time every second, and the sampling rate was 200 samples per second. The control of the whole system and the storage of the data are done by a portable PC. The triggering algorithm is based on the STA/LTA ratio. Station Cartesian co-ordinates were measured with a laser theodolite with respect to a reference benchmark, whose absolute geographic co-ordinates were obtained through GPS positioning. The reference system has the y-axis oriented toward north and the x-axis toward east (Fig. 3).

In order to control possible site effects produced by the caldera structure, two three-component stations were deployed on the compact rock structure of the caldera border. The first one, named station E, was placed on basaltic intrusions of the caldera ring in Las Pilas formation, and the other, named station F, in Montón de Trigo formation, Fig. 2.

3. Data description and spectral analysis

The level of seismic activity registered in the experiment is relatively low in comparison with other volcanoes as Vesuvio (Bianco et al., 1999), Stromboli (Del Pezzo et al., 1998) or Deception Island (Alguacil et al., 1999). During the 40 days of the experiment local, very local earthquakes and artificial explosions were recorded. No typical active volcano events, such as long period events were registered. Together with this set of data, two daily samples of noise were registered during 12 days in the middle of the experiment, at midnight and one hour later. Part of the same data set (seven earthquakes) was used by Del Pezzo et al. (1997) in order to study the wave composition of the coda waves of local earthquakes.

From the whole set of 76 events, we selected 21 records with good signal-to-noise ratio and recorded by both modules of every array. They have been visually classified into three groups: local earthquakes (7 events), very local earthquakes (10 events) and artificial explosions (4 events):

(1) Local earthquakes are characterized by an S–P time between 3 and 6 s (no earthquakes with an S–P

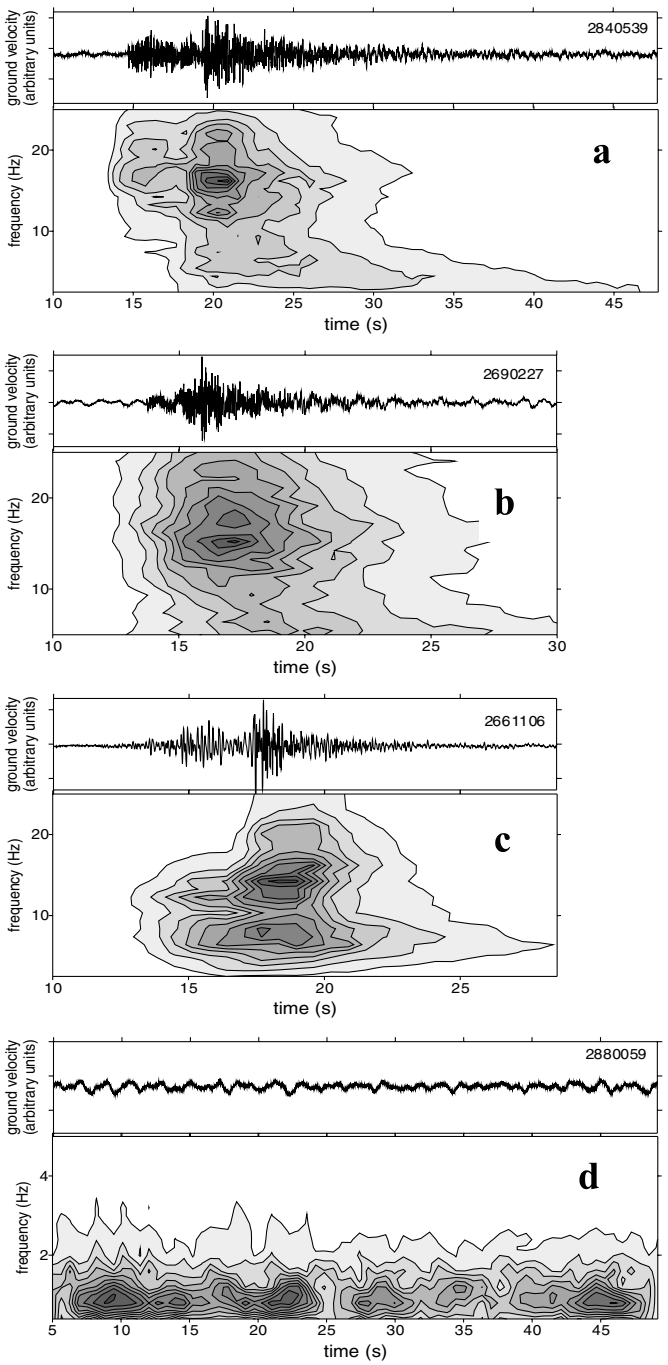

Fig. 4. Seismograms and spectrograms of some events analyzed in the present work. (a) Local earthquake, (b) very local earthquake, (c) artificial explosion, (d) background seismic noise. The vertical scale in the spectrograms of the earthquakes is the same (0–25 Hz) to compare them, although in the case of artificial explosions their spectral contents reach frequencies as high as 50 Hz.

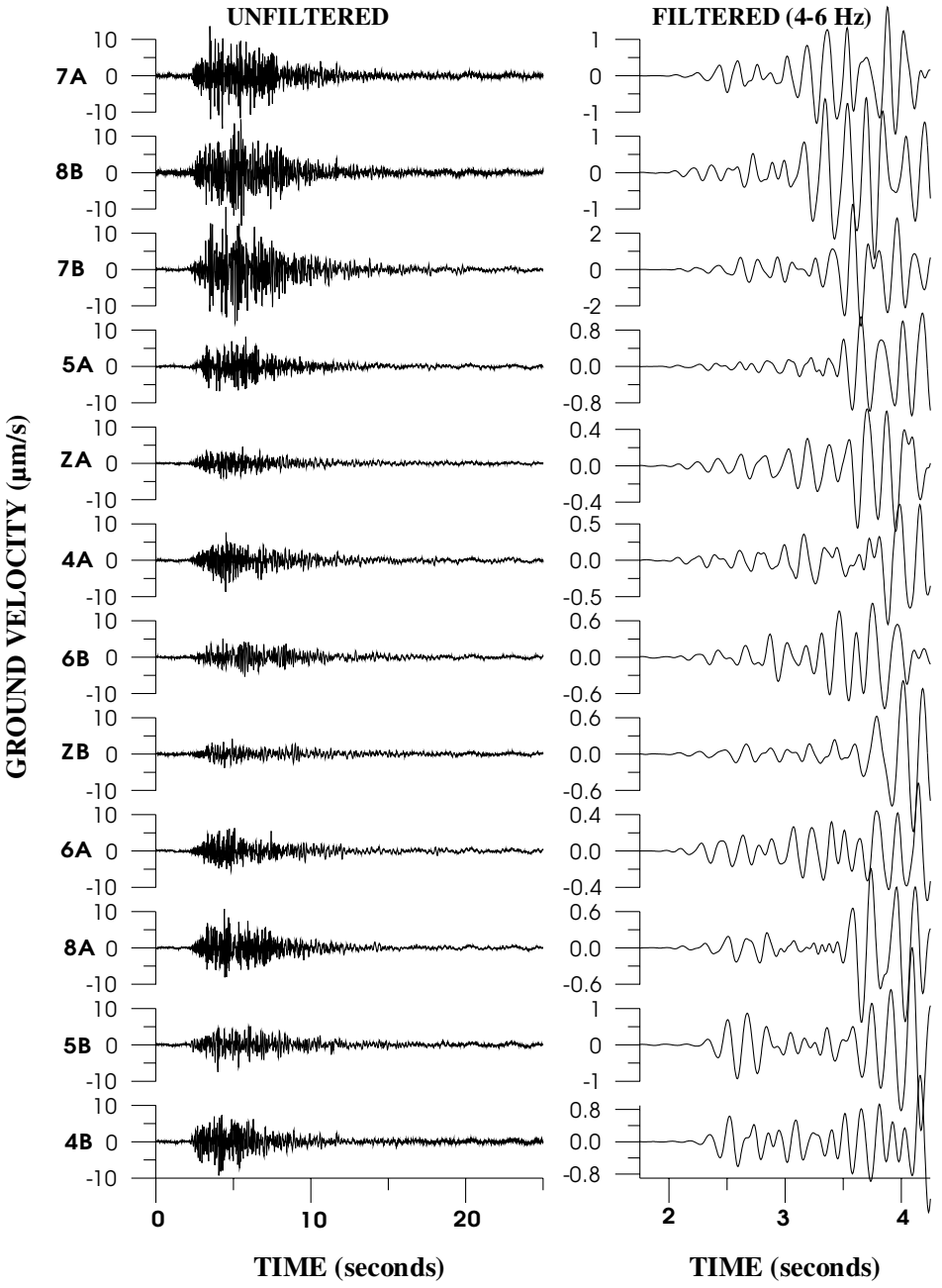

Fig. 5. (Left) An example of a very local earthquake (number 5 in Table 2) for all the array AB stations. The seismograms are presented in real ground velocity (10^{-3} mm/s). Stations are presented according the arrival after the location of the source. (Right) A detail of the first P onset for the same earthquake filtered in the 4–6 Hz band. In this frequency band, the ZLCC presents the better MACC value.

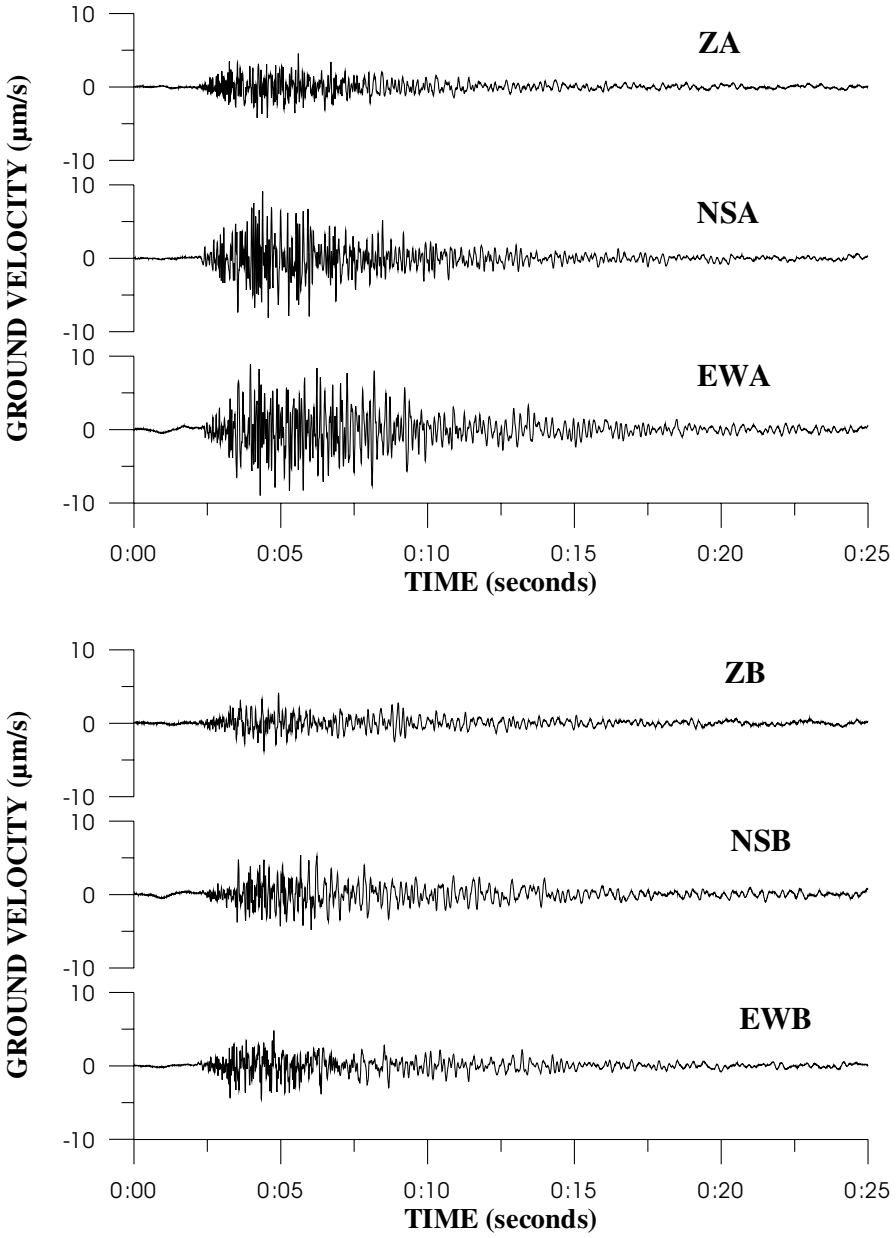

Fig. 6. The same earthquakes recorded in both 3-component stations of array AB.

time greater than 6 s were registered). Their moment magnitude ranged between 2 and 3. The moment magnitude was estimated using the seismic moment. The seismic moment was calculated through the source spectrum. It is possible to use this procedure for these magnitudes and distance when the signal-to-noise ratio is high enough. The spectrogram (Fig. 4a) shows a broad spectral band, from 1 to 25 Hz with no dominant spectral peaks.

(2) Very local earthquakes are characterized by as S–P smaller than 3 s (they could be located inside of the volcano edifice). Their magnitudes are between

Table 1
Frequency bands and window lengths at every frequency

Frequency (Hz)	Band (Hz)	Duration (s)	Frequency (Hz)	Band (Hz)	Duration (s)
1	0.5–1.5	2	6	5.5–6.5	0.35
2	1.5–2.5	1	7	6.5–7.5	0.3
3	2.5–3.5	0.7	8	7.5–8.5	0.3
4	3.5–4.5	0.5	9	8.5–9.5	0.3
5	4.5–5.5	0.4	12	9.5–15	0.3

1.2 and 2.0. These magnitudes where estimated using a duration-magnitude scale. Their spectral contents reach more in high frequencies than those observed in the local earthquakes (Fig. 4b). In Figs. 5 and 6, we plot an example of a very local earthquake (number 5 of Table 2) for all the stations of the array AB.

(3) Artificial explosions are characterized by: no clear onset of S-waves in the horizontal components and a clear secondary impulsive arrival, observed about 5 s after the beginning of the signal, with a visible, on the seismograms, low apparent velocity. They took place only during the day time. Their spectral characteristics are similar to those observed in the local earthquakes. The spectral contents of the secondary impulsive arrivals reach frequencies as high as 50 Hz (Fig. 4c).

During the period of the experiment we registered two samples of noise every day, 65 s long. The spectral content of the seismic noise is very different from that measured for other signals (Fig. 4d). The seismic noise shows a narrow spectral band, with the main part of the energy concentrated at a frequency lower than 2 Hz. The seismic noise spectral shape remained stable in time and sites during the period of the experiment.

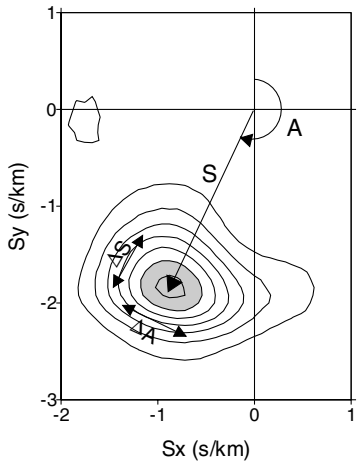

Fig. 7. Graphical example of the procedure we used to calculate back-azimuth (*A*), apparent slowness (*S*) and their related errors in the slowness space (*Sx*, *Sy*).

4. Location of the seismic sources

4.1. Slowness and back-azimuth analysis

We used the "zero-lag cross-correlation" (ZLCC) technique (Frankel et al., 1991) to analyze the waveforms and to locate the seismic sources of the selected events. This method provides a measure of the apparent velocity of the seismic waves, when they cross the array, and of the back azimuth to the associated source. Del Pezzo et al. (1997) have previously applied this technique to seven local events of the present paper. A detailed description of the ZLCC technique is reported by Del Pezzo et al. (1997) and Almendros et al. (1999).

Chouet et al. (1997) pointed out that in the frequency-slowness analysis, the use of several narrow frequency bands provides a stable solution. These authors performed, in order to obtain a unique final solution, a final stacking of the whole set of solutions in every frequency band. Following this criterion, we selected 10 frequency bands, starting from 0.5 to 12 Hz (see Table 1). In every frequency band, the seismograms were filtered by using a four pole Butterworth band-pass filter. Then, the ZLCC technique was applied by using a moving window whose length was dependent on the central frequency of the band pass, as reported in Table 1. The time window length was fixed in order to ensure that inside

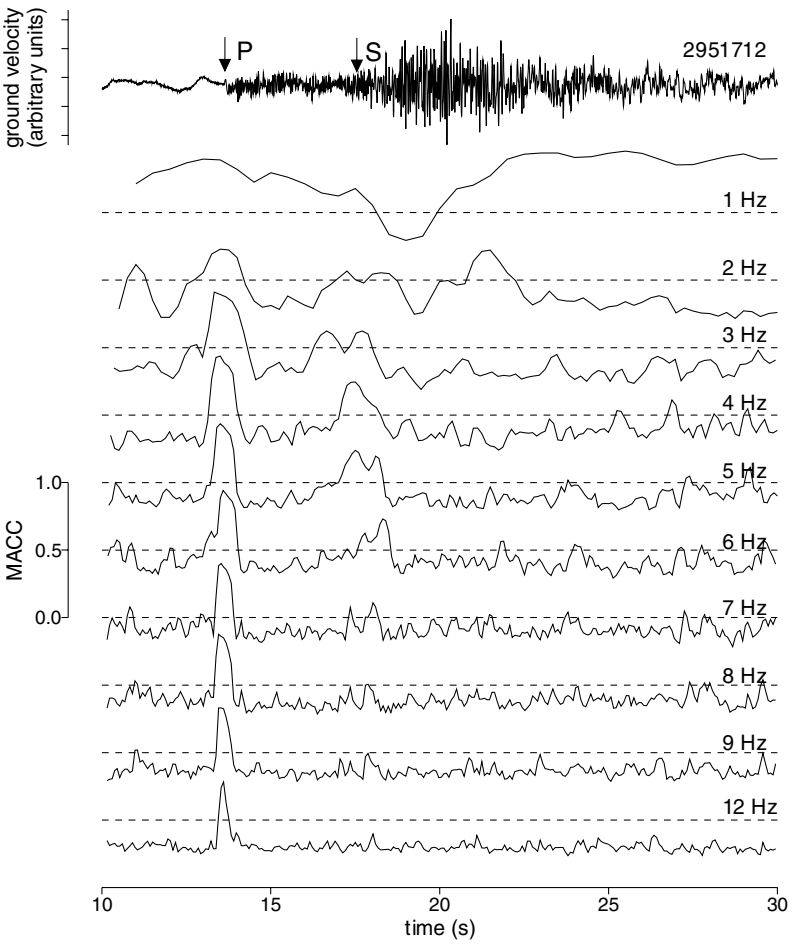

Fig. 8. An example of the time evolution of the MACC value for all the frequency bands. Observed as the P-wave onset at frequencies higher than 2 Hz present well-correlated solution, while the S-wave onset appears well correlated in the frequency bands of 3, 4, 5 and 6 Hz.

of every window there are at least two, and no more than three or four, wave cycles. This window was shifted in time one half window length each step since the pre-event seismic noise until the end of the signal. For each step and frequency band, the maximum averaged cross-correlation value (hereafter MACC) was calculated to obtain the array parameters (apparent slowness and back-azimuth) of the incoming wave front. To obtain these values, we use a grid search method in the parameter space. In the present study, the grid was performed from −4 to 4 s/km, with spacing of 0.04 s/km in the apparent slowness space, described by the two coordinates of the slowness vector (*Sx* and *Sy*). In this process, there are two main sources of errors: one due to the array geometry, time sampling and grid search, and the other due to the seismic noise and the lack of coherence of the signal across the array caused by the propagation factors (ray paths, reflections, etc.). In Fig. 7, we show graphically the procedure to calculate back-azimuth, apparent slowness parameters and related errors.

Due to the short S−P time of the very local earthquakes, the approximation of an incoming plane wave-front could be biased. Almendros et al. (1999) have developed a technique that permits to assume a circular wave-front geometry in the ZLCC method. This approximation has to provide better MACC values when the incoming wave-front fits better to a circular shape than the planar one. We performed a

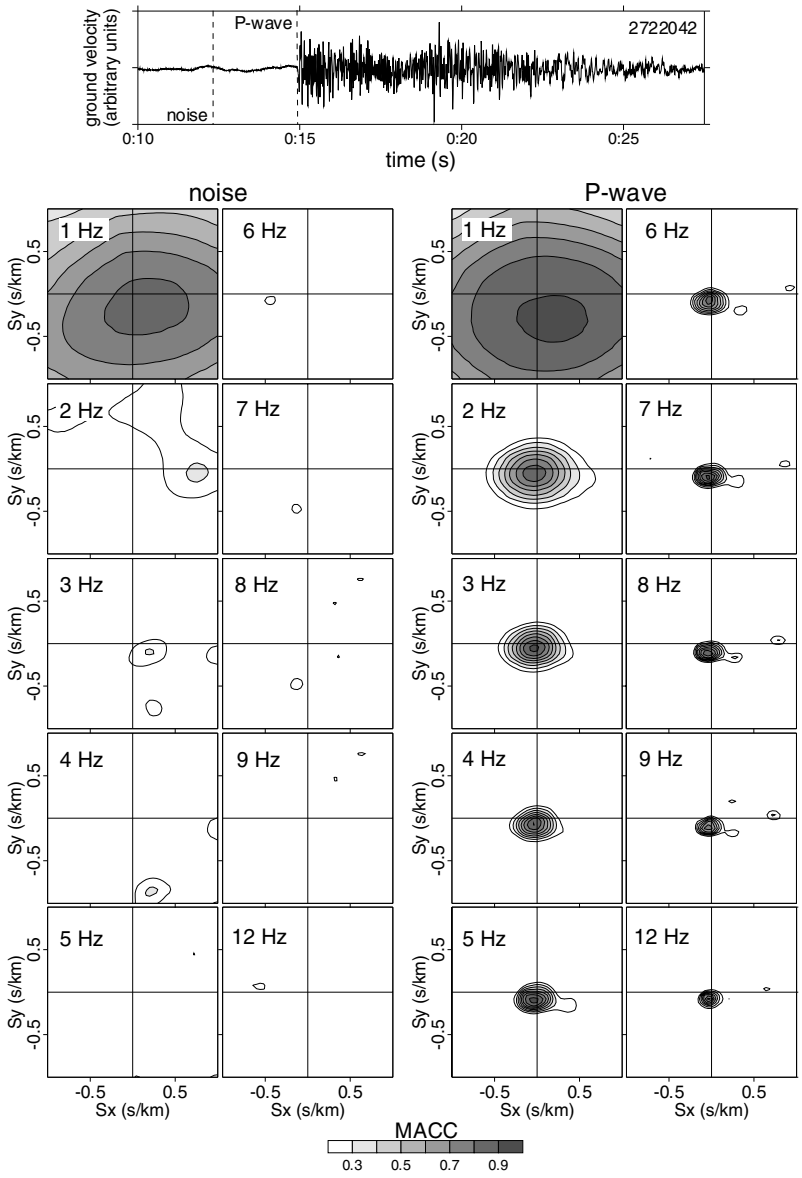

Fig. 9. A graphical example of the staking procedure for the first P-wave arrival time window, and a comparison with the pre-event seismic noise.

test using this technique for the first P onset of a subset of the data. Results do not show improvement of MACC values as compared to the plane wave-front approximation. Therefore, due to its simplicity and computational efficiency, we used the planar geometry in our study.

4.1.1. Analysis of local and very local earthquakes

Slowness and back-azimuth for the earthquakes belonging to the first two classes (local and very local earthquakes) were obtained at all frequency bands for time windows sliding along the whole seismogram. Almendros et al. (1997) empirically fixed

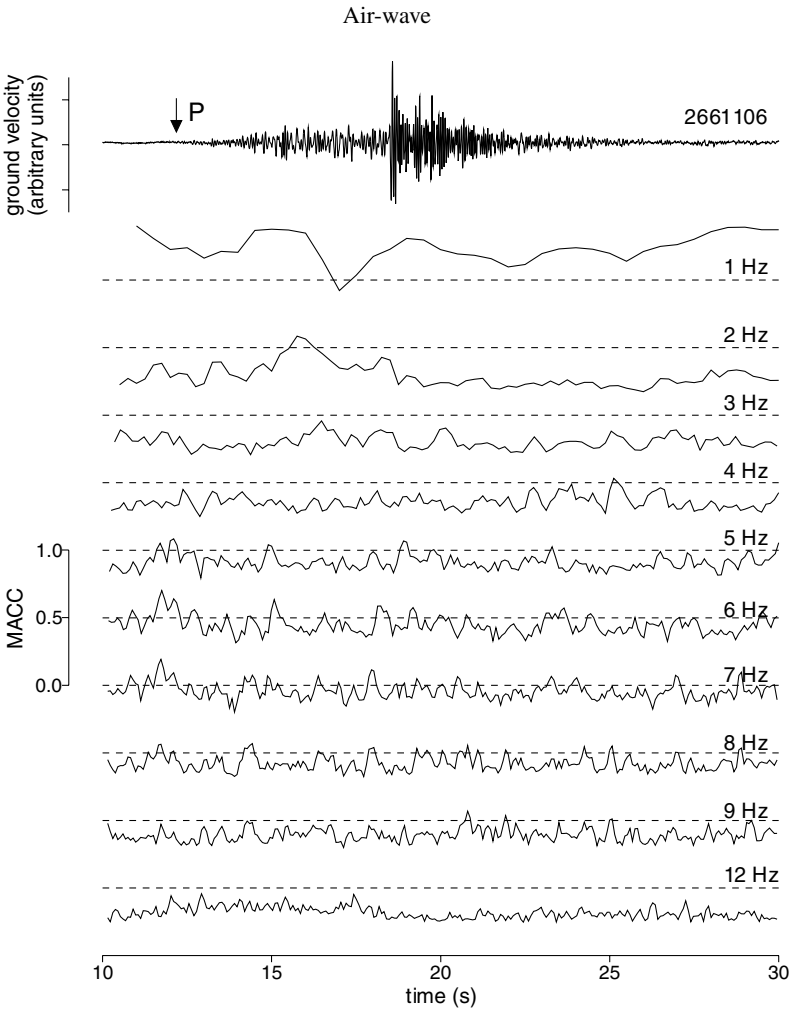

Fig. 10. Same as that of Fig. 8 but in case of an artificial explosion.

the selection threshold for the arrivals of well-correlated phases at a MACC value greater than 0.5. Del Pezzo et al. (1997) discarded all solutions for which MACC value was lower than 0.7. The above criteria were based on the consideration that well-correlated solutions are those that have a MACC value at least two or three times the average value obtained for the pre-event seismic noise. In the present work, we analyzed the pre-event seismic noise of all the earthquakes. Results show that, for the 0.5–1.5 Hz band the average MACC value is 0.8, for the 1.5–2.5 is 0.4 and for the remaining bands is 0.35. Due to the presence of highly correlated seismic noise in the lowest frequency band, we could not consider any solution for that frequency band. Solutions with MACC greater than 0.8 were considered for the second frequency band, and greater than 0.7 for the rest of them. After this type of filter, only the time windows around the first onset of the P waves and some S arrivals fulfilled this criterion. No other well-correlated arrivals appear in the seismograms. In Fig. 8, we show an example of the time evolution of the MACC value for all the frequency bands. The P onset at frequencies higher than 2 Hz presents a well-correlated solution, while the S onset appears well correlated in the frequency bands of 3, 4, 5 and

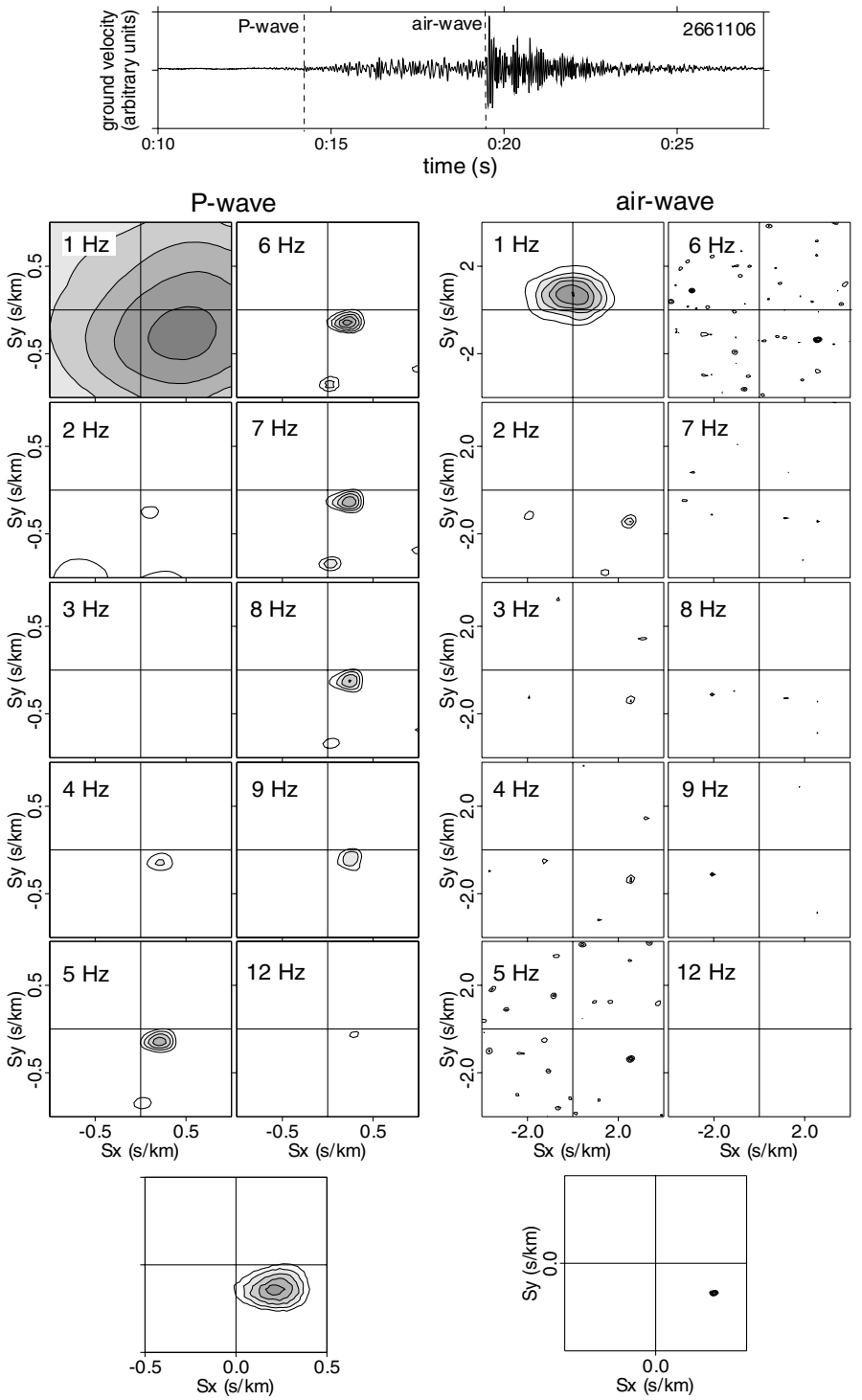

Fig. 11. Same as that of Fig. 9, showing the staking procedure for the first P-wave onset and the secondary impulsive arrival in case of an artificial explosion.

Table 2
Results of the array analysis of the selected earthquakes and explosions (S = apparent slowness; A = back-azimuth; solution between the error limits; events 18, 19 and 20 are artificial explosions)

Number	Date	Array AB						Array CD					
		S (s/km)			A (°N)			S (s/km)			A (°N)		
1	2601203	0.06	0.13	0.21	81	95	101		–			–	
2	2651408	0.16	0.18	0.20	247	255	258		–			–	
3	2690227	0.14	0.17	0.20	235	241	244	0.06	0.36	0.57	249	274	290
4	2700026	0.13	0.16	0.19	238	249	254		–			–	
5	2710322	0.22	0.34	0.45	80	85	89	0.11	0.39	0.57	38	61	75
6	2710336	0.20	0.43	0.65	78	91	96		–			–	
7	2722042	0.07	0.11	0.15	172	197	208		–			–	
8	2782106		–			–		0.00	0.09	0.28	109	207	248
9	2791809	0.10	0.14	0.19	240	249	252		–			–	
10	2840539	0.04	0.11	0.18	88	99	104		–			–	
11	2870324	0.05	0.10	0.18	54	74	82		–			–	
12	2880052		–			–		0.16	0.52	0.67	231	251	265
13	2881733	0.04	0.10	0.16	80	97	105		–			–	
14	2902236	0.07	0.13	0.19	223	229	232	0.00	0.25	0.45	254	283	296
15	2951712	0.04	0.15	0.32	60	94	109		–			–	
16	2630024	0.24	0.34	0.44	118	129	133	0.14	0.25	0.36	71	83	88
17	2630742	0.15	0.28	0.42	70	74	76		–			–	
18 (P)	2661033	0.69	0.94	1.22	95	126	140		–			–	
19 (P)	2661053		–			–		0.39	0.69	1.00	66	81	87
20 (P)	2661106	0.22	0.24	0.30	116	121	130	0.43	0.52	0.61	77	84	87
18 (air)	2661033	2.90	3.04	3.10	110	117	130		–			–	
20 (air)	2661106	2.86	2.90	2.97	116	118	120		–			–	
21 (air)	2731050	2.91	2.94	3.01	130	133	134		–			–	

6 Hz. An unique final solution was obtained, to every earthquake, by staking all the solutions with MACC values higher than the cut-off one at different frequency bands. In Fig. 9, we show a graphical example of the application of this procedure for the first P-wave arrival time window. In the same figure, a comparison with the pre-event seismic noise is also reported. Due to the high MACC value for the seismic noise in the 0.5–1.5 band, we did not consider this band in the final stacking procedure. The back-azimuth and the apparent slowness for the first P-wave time window was estimated for every earthquake from the final stacked solution. The results for the analyzed earthquakes are reported in Table 2.

Table 3
Results of the joint location (D = distance, A back-azimuth)

Number	Array AB		Array CD	
	A (°N)	D (km)	A (°N)	D (km)
3	241	4.0	274	3.1
5	85	4.2	61	5.2
14	229	2.7	283	1.7
16	129	2.9	83	2.6
20	121	3.5	84	3.4

4.1.2. Artificial explosions

The same kind of analysis was applied to the data classified as artificial explosions. The possible position of the source of these explosions is a military field located near the array AB site. This field is in the external border of the Cañadas caldera. An example is reported in Fig. 10 for the entire signal and for all the frequency bands. The first P-wave arrival of the explosions shows a MACC value higher than the threshold at 5, 6 and 7 Hz. The impulsive phase (marked as air wave in the plot) shows a MACC value close or below the cut-off value. Following the same criterion used for earthquakes, only the

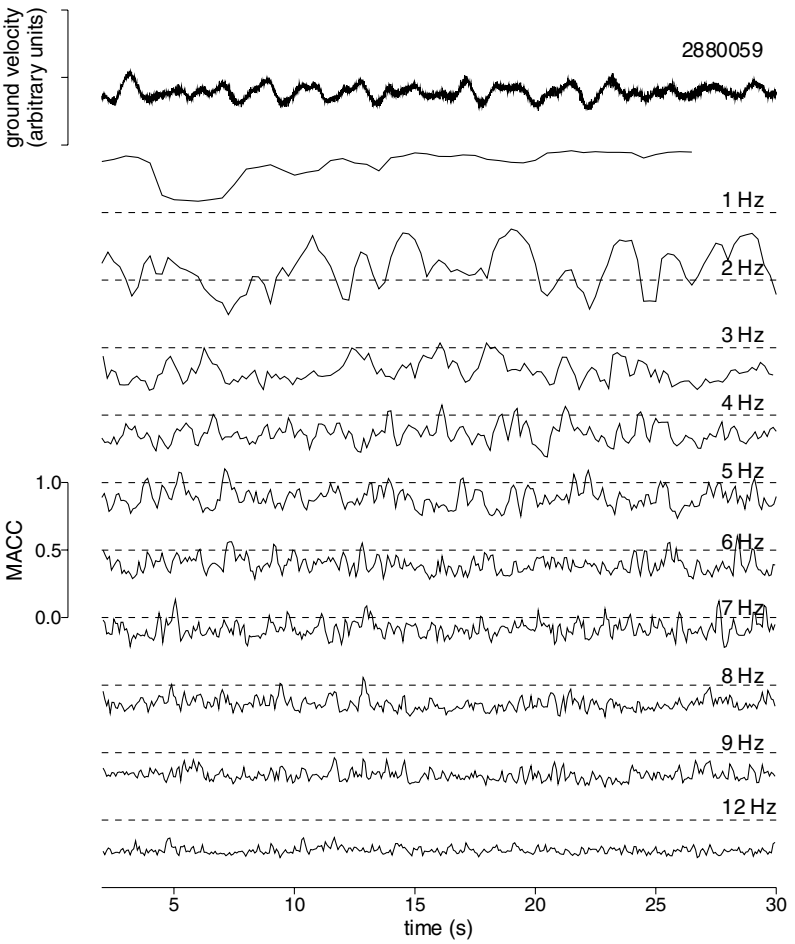

Fig. 12. Same as that of Figs. 8 and 10 but in case of a sample of background seismic noise.

P-wave onset in the 5, 6 and 7 Hz frequency bands could be considered as coherent arrival. In Fig. 11, we show an example of the application of the ZLCC technique to the first P-wave time window and to the window corresponding to the presumed air-wave, together with the stacked solution. As can be observed, the staked solution indicates a clear and unique solution both for P-waves and for the impulsive arrival, possibly the air-wave. The first arrival shows an apparent slowness relatively high (an apparent velocity between 1 and 4 km/s), while the presumed air-wave shows an apparent slowness of 2.95 s/km (an apparent velocity of 340 m/s, see Table 3). The particle motion analysis reveals a complex pattern for both the P-wave and for the airwave. The particle motion for the first P-wave onset shows a complex pattern, far from the expected pattern of a far field P-wave. This pattern could be expected in case of a very shallow artificial explosion, due to the complex surface structure that can modify the wave field. The low observed correlation for the airwave, although characterized by a clear impulsive arrival, could be due to the short wave length of the signals. In fact, at the frequencies in which we clearly observe the airwave (8 Hz and higher) the wavelength of the signal is around 40 m. As the aperture of the array CD is 400 m and that of the array AB is 600 m, there is a loss of coherence for the wave packet crossing the array. A similar interpretation can be done for the S-wave time window of the local earthquakes, for which the observed wavelength is smaller than the array aperture at high frequencies.

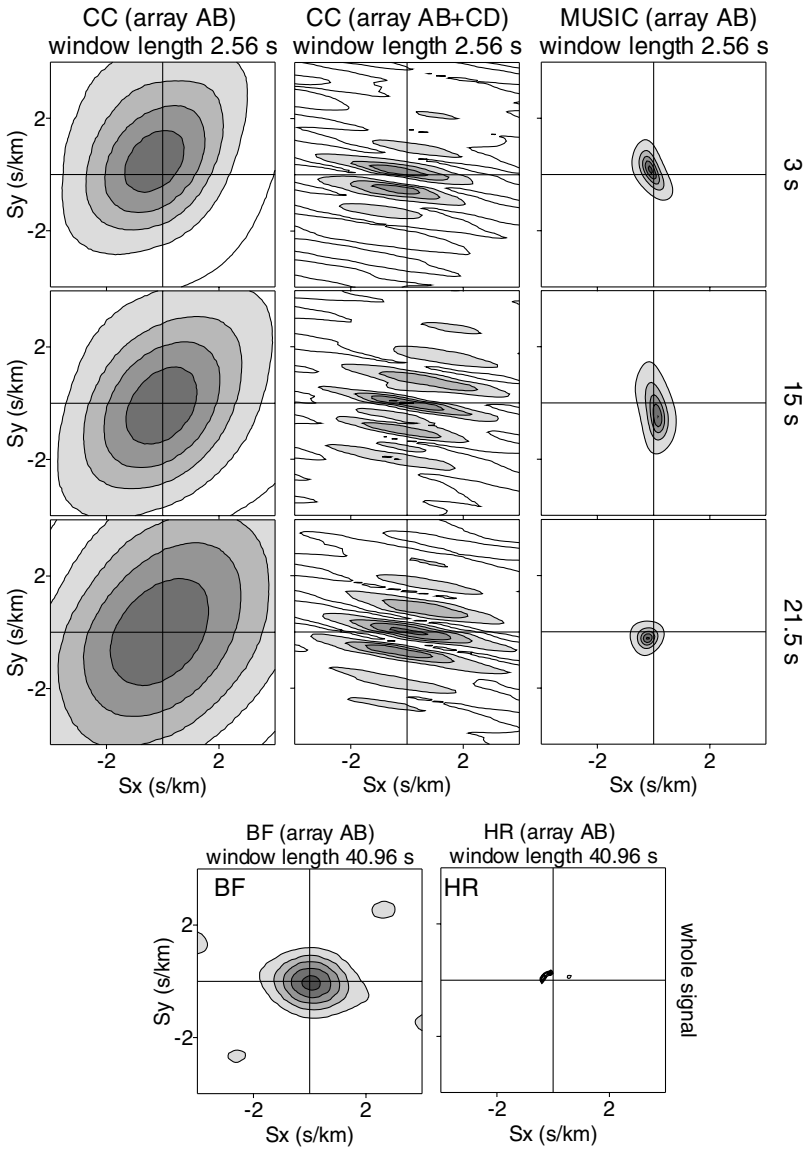

Fig. 13. Comparison of the analysis of the background seismic noise by using different array techniques. In case of the ZLCC and MUSIC techniques, we analyzed three windows of noise with the same window length. In case of High-Resolution and Beam Forming techniques, we analyzed the whole seismogram.

4.1.3. Seismic noise

We recorded two samples of noise every night during 12 days, with the aim of observing if it is correlated or incoherent. If the seismic noise is coherent, it could track the volcanic tremor source. The experiment was done during night time in order to reduce as much as possible the effect of the cultural noise. In other volcanoes, like Stromboli for example, the analysis of the background noise has revealed the presence of volcanic tremor in the 1 Hz frequency band (Chouet et al., 1997) and the presence of ocean microseism at lower frequencies (Braun et al., 1996). We proceeded to analyze the background noise at Teide with the same procedure followed in the analysis of the

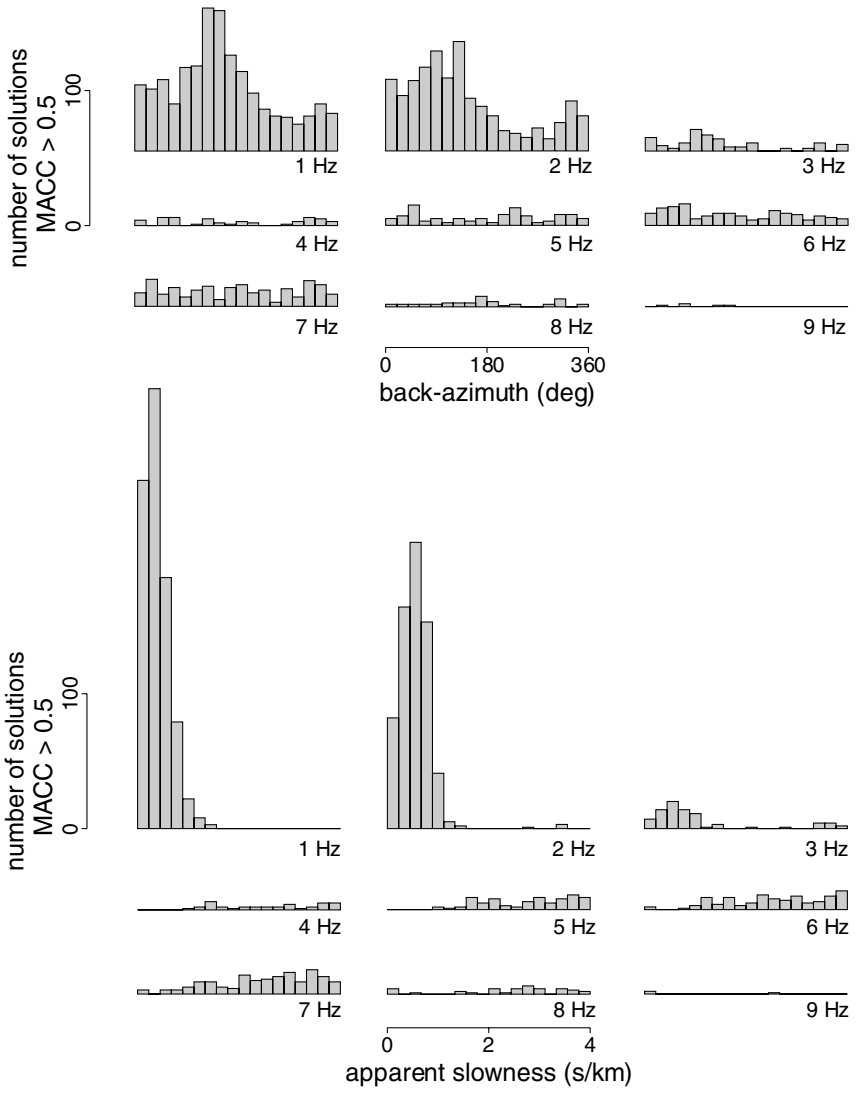

Fig. 14. Bar diagrams of the distribution of the back-azimuth (up) and apparent slowness (down) for the whole set of background seismic noise data.

earthquakes and explosions. In Fig. 12, we show an example of the evolution of MACC value against frequency and time along the signal. In Fig. 13, we provide an example of the analysis in the apparent slowness plane for a sample of noise. As can be observed that from Fig. 12, only in the lowest frequency bands (0.5–1.5 and 1.5–2.5 Hz) the main part of solutions present a MACC value higher than the threshold. In some cases, this MACC value is close to 0.95, higher than that obtained for the P-wave arrivals of the local earthquakes. For the other frequency bands, the solutions show low MACC values, representing the arrival of incoherent waves. In order to exclude any possible bias generated by the used method, we compared the solutions obtained using the ZLCC method with the ones provided by the High Resolution (Capon, 1969), Beam Forming (LaCoss et al., 1969) and MUSIC (Schmidt, 1986) technique applied to the same data set. We compared also the solutions obtained with the ZLCC method by

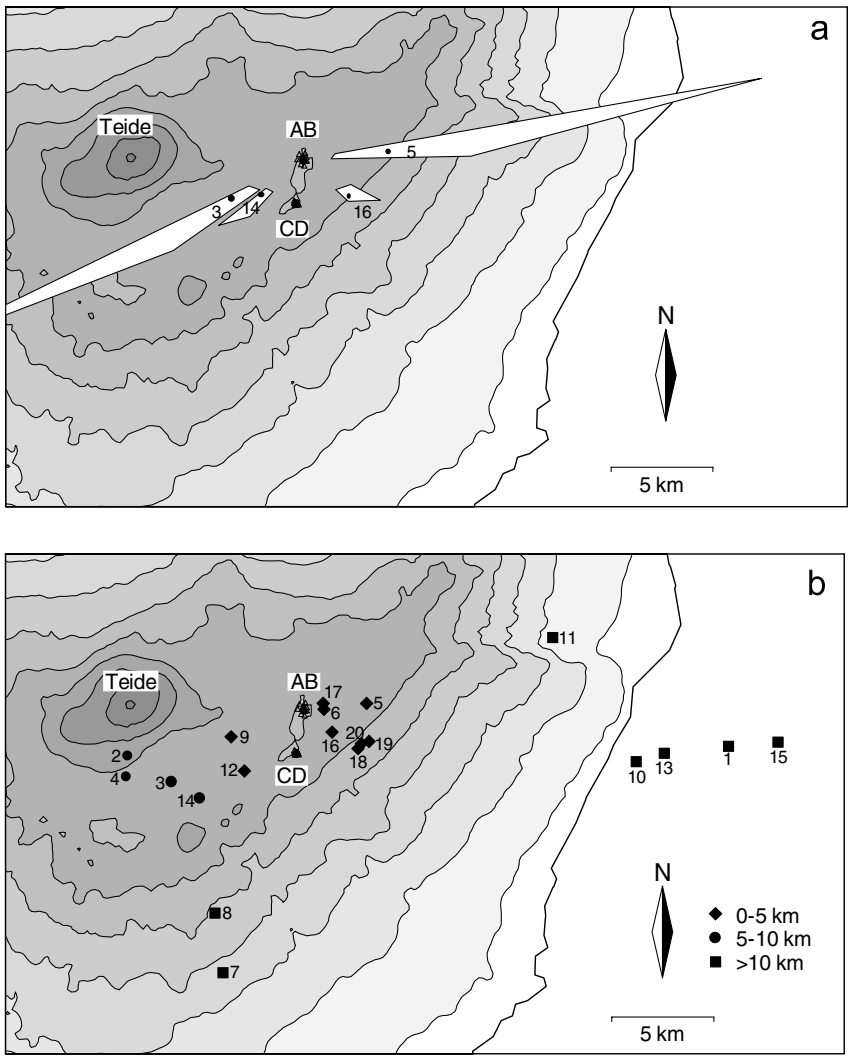

Fig. 15. Epicentral maps of the seismicity located in the present work. The numbers plotted in both maps are the same shown in Tables 2 and 3. (a) Earthquakes located by using the joint location procedure. The white area is the maximum error area obtained by a graphical procedure. (b) Earthquakes located by the ray tracing procedure. Symbols are related with the focal depth.

using the array AB with those obtained by using simultaneously both arrays. This comparison is shown in Fig. 13. In case of ZLCC and MUSIC, we analyzed three windows of noise with the same window-length. In case of High Resolution and Beam Forming, we analyzed the whole seismogram. As can be observed all the used methods provide the same back-azimuth and apparent slowness. The complex shape observed in the solutions of ZLCC method by using simultaneously both arrays is due to the effect of spatial aliasing. The test reveals the stability and the reliability of the estimates obtained with the ZLCC method, confirming the arrival of coherent phases in the background noise at low frequency.

The distribution of the apparent slowness and back-azimuth for the whole set of background noise data, is shown in Fig. 14. We report for all the frequency bands those with MACC value higher than 0.5. From the diagrams we infer that:

Table 4
Velocity of the IGN model (Z = layer depth; V_p = P-wave velocity; V_s = S-wave velocity)

Z (km)	V_p (km/s)	V_p/V_s
4	4.2	1.75
12	6.3	1.75
18	7.5	1.75
∞	8.0	1.75

(1) The frequency bands 0.5–1.5 Hz and 1.5–2.5 Hz are the most populated. The number of solutions with MACC > 0.5 decreases with the frequency.

(2) In the two lowermost frequency bands, the distribution of apparent slowness is peaked at low slowness values, that corresponds to very high apparent velocity.

(3) In the high-frequency bands, the apparent slowness distribution shows an higher percent of apparent velocities close or smaller than 1 km/s.

(4) At all frequency bands, the back-azimuth distribution seems to be uniform, with no dominant direction.

(5) Particle motion plots, carried out on the noise, show a complicated pattern in the lowermost frequency bands.

From these observations, the following hypotheses can be drawn:

(a) The coherent arrivals at low frequencies (0.5–1.5 and 1.5–2.5 Hz) represent some kind of waves with a vertical incidence.

(b) At high frequencies the solutions are compatible with the arrival of surface waves, possibly generated by strong scattering processes at the surface, related to the presence of surface topography irregularities, as also observed elsewhere (Del Pezzo et al., 1997; Chouet et al., 1997).

(c) From the present analysis, it is hard to infer the nature of the waves composing the low-frequency noise. The vertical incidence of the seismic noise waves could explain the broad azimuthal distribution observed in the present work.

Table 5
Velocity of ETNA model (Z = layer depth; V_p = P-wave velocity; V_s = S-wave velocity)

Z (km)	V_p (km/s)	V_p/V_s
0.02	0.7	1.43
0.5	1.8	1.73
1.0	2.2	1.73
1.5	2.8	1.73
2.0	3.8	1.73
4.0	5.0	1.73
20.0	6.0	1.73
∞	8.0	1.73

Table 6
Velocity of DECEPTION model (Z = layer depth; V_p = P-wave velocity; V_s = S-wave velocity)

Z (km)	V_p (km/s)	V_p/V_s
0.02	0.5	1.43
0.57	1.5	1.60
1.41	1.8	1.65
6.0	4.5	1.73
12	6.0	1.73
25	7.6	1.73
∞	8.2	1.73

4.2. Determination of the epicentral distance and focal depth

4.2.1. Joint location using both seismic antennas

Some of the earthquakes and explosions were recorded simultaneously by the two seismic antennas. Determining the back-azimuth in both of them, the epicentral area can be obtained from the intersection of both directions, together with the error interval. The error can be estimated simply propagating the uncertainty in the back-azimuth direction into the coordinates of the intersection between the two back-azimuth lines. The error field is not uniform, depending on source distance and relative position respect to the two array centers. It is maximum for back-azimuths in the same direction of the lines connecting the two array centers. This analysis yields an epicentral position independent of the velocity model, provides that lateral heterogeneity do not introduce misfit of the propagation azimuth with respect to the source location. In the present work, seven earthquakes and one explosion were recorded simultaneously by both seismic arrays (see Table 2). Only five of them (four earthquakes and the explosion) can be located with this procedure. Earthquakes numbers 10, 11 and 13 of Table 2 have no solutions from the array CD. In Table 3, we reported the estimated distance and in Fig. 15a we plotted the position,

Table 7
S–P time (s) and results of the ray-tracing procedure using the three different velocity models (D = epicentral distance; Z = depth; NS = no solution)

Number	S–P time		Ray-tracing using the IGN model				Ray-tracing using the ETNA model				Ray-tracing using the ETNA model			
	Array AB	Array CD	Array AB		Array CD		Array AB		Array CD		Array AB		Array CD	
			D (km)	Z (km)	D (km)	Z (km)	D (km)	Z (km)	D (km)	Z (km)	D (km)	Z (km)	D (km)	Z (km)
1	5.0	–	32.0	16.1	–	–	20.9	18.8	–	–	28.9	14.8	–	–
2	2.4	–	7.7	6.6	–	–	8.9	5.8	–	–	7.2	6.2	–	–
3	2.2	1.8	6.5	6.4	NS	NS	7.4	5.9	3.1	2.6	6.1	6.1	2.1	2.6
4	2.1	–	6.0	6.7	–	–	9.3	5.7	–	–	7.9	6.8	–	–
5	1.3	1.7	NS	NS	NS	NS	3.1	1.7	3.1	2.1	1.4	2.0	2.1	2.4
6	0.5	–	NS	NS	–	–	1.0	0.6	–	–	0.7	0.8	–	–
7	3.9	–	20.7	19.5	–	–	13.5	17.1	–	–	17.8	18.3	–	–
8	–	3.2	–	–	13.5	19.0	–	–	8.8	15.3	–	–	11.1	17.4
9	1.3	–	4.9	5.1	–	–	3.8	4.6	–	–	2.5	4.0	–	–
10	4.7	4.6	25.4	22.7	–	–	16.5	20.5	–	–	22.9	21.7	–	–
11	4.0	4.0	19.6	21.9	–	–	12.7	18.6	–	–	16.9	20.4	–	–
12	–	1.6	–	–	NS	NS	–	–	2.7	1.0	–	–	2.7	1.4
13	5.4	5.7	27.6	28.1	–	–	17.8	25.4	–	–	25.0	27.3	–	–
14	1.9	2.0	8.2	7.9	NS	NS	6.7	7.4	6.2	3.2	5.6	7.6	1.6	3.3
15	4–8	–	26.5	12.1	–	–	23.3	13.8	–	–	22.0	14.4	–	–
16	0.9	1.6	NS	NS	NS	NS	1.8	1.3	3.6	2.3	1.0	1.5	1.3	2.7
17	0.6	–	NS	NS	–	–	1.0	1.3	–	–	0.6	1.1	–	–

Table 8
Epicentral distance for the explosions with ETNA model (Air-P = time air-P; D = distance)

Number	Air-P (s)	D (km)
18	5	3.3
19	5.5	3.9
20	11	7.3

together with the error area for the four analyzed earthquakes. The fact that the epicentral solution for the explosion is on the military field suggests that lateral heterogeneities do not affect strongly the ZLCC solutions.

The solutions obtained with this method are independent on the velocity model and on the seismic phase selected for the analysis. In principle, the method can be applied to volcanic tremor too, in the hypothesis that the same coherent wave front crosses both the arrays coming from a unique source.

4.2.2. Ray tracing

Utilizing the estimate of slowness and back-azimuth for two seismic phases (e.g. P and S for earthquakes, or P and airwaves for explosions) and assuming a velocity model of the region, it is possible to estimate distance and depth of the earthquake. From the S–P time, it is simple to estimate the distance along the ray connecting the source to the receiver. The estimate of the ray parameter will fix the depth. In case of artificial explosions, the onset of the airwave can be used instead of the S onset, together with the assumption of a source located at surface. In this case, we can estimate the epicentral distance by using the expression:

$$D = \frac{t_{\mathrm{air}} - t_{\mathrm{p}}}{s_{\mathrm{air}} - s_{\mathrm{p}}}$$

D is the epicentral distance, s_{p} the apparent slowness of the P-waves, s_{air} the apparent slowness of the airwave and $(t_{\mathrm{air}} - t_{\mathrm{p}})$ the interval between both signals.

In Teide area there is not a specific velocity model that could take into account the volcanic origin of the upper three kilometers. Furthermore, in the area there are no enough tomographic models in detail that could permit a 3D ray-tracing. Therefore, in order to estimate the focal position of the analyzed earthquakes, it is necessary to assume a 1D velocity model. The velocity model used by the Spanish Seismic Network, named hereafter IGN (Table 4) does not take into account details of the upper layers. To take into account the volcanic nature of the upper part, it is necessary to use models developed in other volcanic areas. In the present analysis we will use two models. The first velocity model was determined for the Etna Volcano and used by several authors such as Scarpa et al. (1983), hereafter ETNA (see Table 5). Both, Teide and Etna Volcanoes share some geologic characteristics, as to be strato-volcanoes or others. The second model was used by Ibáñez et al. (1997) at Deception Island Volcano (Antarctica), named hereafter DECEPTION (Table 6). This model was based on field experiment and on seismic profiles of the area. The S–P time and AIRWAVES–P time are reported in Table 7. Epicentral distance and focal depth for all the earthquakes previously analyzed with the ZLCC method are also reported in Table 7 and in Table 8 for the explosions. The results can be summarized as:

(1) Those earthquakes with apparent velocity smaller than 4 km/s cannot be located by the IGN model.

(2) The DECEPTION and ETNA models seem to provide more consistent results than the IGN model. There are no strong differences in the location provided by both of them.

(3) The ETNA model seems to be more adapted than the DECEPTION model to locate the recorded seismicity because the DECEPTION model is associated to a region with a tectonic characteristic different than the Canary Islands.

The error area of these locations is related with the following parameters:

(1) the velocity model used;

(2) the error estimated in the apparent velocity;

(3) the error estimated in the back-azimuth;

(4) the error in the estimation of the interval (S–P) and $(t_{\mathrm{air}} - t_{\mathrm{p}})$ intervals.

Taking into account these parameters, we calculated the error interval for the local and very local earthquakes. In case of very local earthquakes the average error interval is ± 2 km in depth and ± 1.5 km in distance. For local earthquakes was ± 5 km in depth and distance. In Fig. 15b, we plot the hypocentral distribution of the seismicity analyzed in the present work and located by using ray tracing

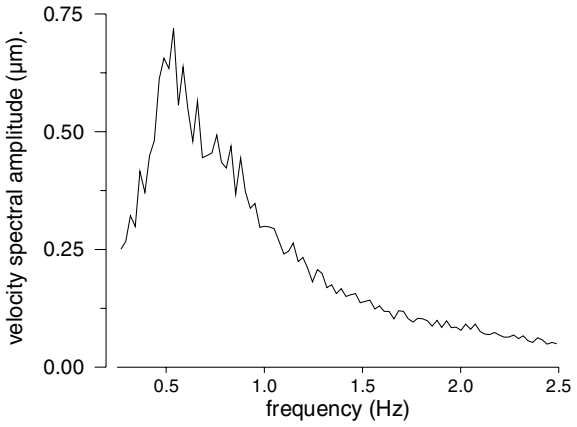

Fig. 16. Array average spectra of a sample of background seismic noise.

and the ETNA model. As can be observed, the earthquakes are located inside the volcanic edifice or close to the caldera border and in the limit of the island.

5. Discussion

5.1. Local seismicity and explosions

The present analysis reveals the existence of moderate local and very local seismicity in the Teide volcano. We analyzed 17 earthquakes from a set of 76 events recorded in a 40 days of seismic survey. The Spanish Seismic Network has located only three of them, earthquakes, 1, 10 and 13 of Table 2. In relation to the distribution of the seismicity we can observe three source areas:

(a) Seismicity located below the volcanic edifice: all the earthquakes associated with the inner part of the caldera are deeper than 5 km and close to 10 km, except earthquakes number 9 and 12. In this area and in this depth, Martí et al. (1995) located the possible place of the magmatic reservoir responsible of the last explosive eruption, the Montaña Blanca eruption 2020 years bp.

(b) Microseismicity related to the border of the Cañadas edifice: close to this area is located the fracture associated to the 1704–1705 eruptions and to the current thermal anomalies in ground-water (Valentín et al., 1990). The earthquakes that could be related to these fractures have a shallow focal depth (around 3 km).

(c) Local seismicity located in the border of Tenerife Island: these earthquakes could be related to the regional seismicity reported in other studies (Canas et al., 1998). The location provided by the regional seismic network to three of them is around the co-ordinates $-16°15'$ longitude west and $28°12'$ latitude north (see Fig. 1). In the present work, the local earthquakes are located closer to Tenerife Island (even by using the IGN model). The difference between both solutions could be due to the lack of seismic stations in the area to poor quality of the three component stations, and to the low magnitude of the earthquakes analyzed here.

The earthquakes belonging to group (a) and (b) can be interpreted as volcano-tectonic seismicity because they are located just in the volcanic edifice with a focal depth smaller than 10 km. From the set of data recorded during the experiment, there is no evidence of low-frequency events. The third set of earthquakes (seven events), located outside from the volcanic edifice shows a location different from that provided by the National Agency. Our data show that more stations are needed in the area for a unbiased location of the regional seismicity and that the geodynamical interpretation of the island is actually based on a possible biased set of epicentral solutions.

The seismic antenna has been able to locate and identify the presence of artificial explosion in the middle of the set of recorded earthquakes. This evidence, based mainly on the identification of airwaves measuring their apparent velocity and back-azimuth, could be useful in volcano seismicity. This identification was possible due to the use of the stacking procedure. The present data show that array techniques could be used, not only to locate the position of the seismo-volcanic source, but are also useful to find constraints on the nature of the radiated wave-field.

5.2. Seismic noise

The array analysis carried out on 12 days of samples of seismic noise recorded at Teide Volcano shows that, for frequencies greater than 3 Hz, the background noise is mainly composed by incoherent phases. The wave-packets that arrive to the array with

some sort of coherence, show a random back-azimuth distribution and an apparent velocity smaller than 1 km/s. These arrivals have been interpreted in other studies, as Spudich and Botswick (1987) or Del Pezzo et al. (1997) as strongly scattered signals probably related to the presence of surface heterogeneities in the area.

In the low-frequency range, basically in the 0.5–1.5 Hz but also in the 1.5–2.5 Hz, we observe the arrival of well-correlated phases. The main characteristic of these arrivals is their high apparent velocity, and their uniform back-azimuth distribution. The particle motion shows a complex pattern, without any clearly defined type of seismic wave. The energy of these waves is so high that their amplitude is greater than the amplitude of the seismic waves from $M = 2$ earthquakes at 20 km. Spectral analysis (in Fig. 16 we show an array average spectra of a sample of noise) shows that the background seismic noise has a broad peak centred on 0.5 Hz. Similar characteristic has been observed in other volcanic islands as Stromboli (Braun et al., 1996) or Hawaii (B. Chouet, pers. commun.). We interpret this background noise as due to the effect of the Oceanic Load. Braun et al. (1996) for Stromboli reported similar results. During the period of the experiment, the local weather was very stable with calm and sun, never perturbed by the arrival of low-pressure fronts, so we exclude any atmospheric cause. Independently on the interpretation the background noise level is high enough to interfere with other seismic waves in the same frequency ranges. This evidence shows that in case of swarms of long-period signals as volcanic tremor or long-period events, that have a typical peak between 0.5 and 3 Hz (Chouet 1996), care must be taken in separating their low-frequency spectral band from the background seismic noise.

6. Conclusions

In conclusion, the volcano-tectonic seismicity detected in the Teide and Cañadas edifice is, at the present, the only clear indicator of the low volcano activity of the island. The location of these earthquakes shows that there is activity below the complex Teide–Pico Viejo and in the external border of the caldera, possibly related with the fracture conduits of the 1704–1705 eruptions. The local seismicity has been located in the border of the island differently from the location reported by the National Seismic Network. A more dense seismic network could be important in the future for unbiased locations which would improve the geological interpretations of the region.

The observed strong background noise at low frequencies, interpreted as generated by Oceanic Load, is too big to permit to detect other signals at these frequencies. The detection and analysis of weak volcanic signals in the frequency range between 0.3 and 1.5 Hz in the Cañadas area would be a difficult task.

Acknowledgements

We are grateful to Bernard Chouet and Gilberto Saccorotti for their comments and constructive reviews. The authors wishes to thank to two anonymous reviewers for their critical reviews and comments. The present work has been partially supporter by the project “European Laboratory volcanoes: Teide. Definition of the fine structures and the plumbing system aimed at eruption prediction, hazard assessment and eruptive mechanism understanding”, EVOV-CT93-0283 CEE, by the project ANT98-1111 and by the “Grupo de Investigación en Geofísica, J.A. RN104.

References

Ablay, G.J., Ernst, G.G.J., Martí, J., Sparks, R.S.J., 1995. The subplinean eruption of Montaña Blanca, Tenerife. Bull. Volcanol. 57, 337–355.

Ablay, J., Martí, J., 1995. Stratigraphy and structure of the Teide–Pico Viejo volcanic complex. In: Martí, J., Mitjavila, J. (Eds.), A Field Guide to the Central Volcanic Complex of Tenerife (Canary Islands). Serie Casa de los Volcanes, vol. 4. Servicio de Publicaciones del Cabildo Insular de Lanzarote, pp. 47–80.

Alguacil, G., Almendros, J., Del Pezzo, E., García, A., Ibáñez, J.M., La Rocca, M., Morales, J., Ortiz, R., 1999. Observations of volcanic earthquakes and tremor at Deception Island — Antarctica. Ann. Geofis. 42, 417–436.

Almendros, J., Ibáñez, J.M., Alguacil, G., Del Pezzo, E., Ortiz, R., 1997. Array tracking of the volcanic tremor source at Deception Island, Antarctica. Geophys. Res. Lett. 24, 3069–3072.

Almendros, J., Ibáñez, J.M., Alguacil, G., Del Pezzo, E., 1999. Array analysis using circular wave-front geometry: an applica-

tion to locate the nearby seismo-volcanic source. Geophys. J. Int., 136.

Ancochea, E., Fuster, J.M., Ibarrola, E., Coello, J., Hernán, F., Cendrero, A., Cantagrel, J.M., Jamond, C., 1990. Volcanic evolution of the island of Tenerife (Canary Islands) in the light of new K–Ar data. J. Volcanol. Geotherm. Res. 44, 231–249.

Bianco, F., Castellano, M., Del Pezzo, E., Ibáñez, J.M., 1999. Attenuation of the short period seismic waves at Mt. Vesuvius, Italy. Geophys. J. Int. 138, 67–76.

Blanco, I., 1997. Análisis e interpretación de las anomalías magnéticas de tres calderas volcánicas: Decepción (Shetland del Sur, Antártida), Furnas (San Miguel, Azores) y Las Cañadas del Teide (Tenerife, Canarias). tesis Doctoral, Universidad Complutense de Madrid.

Braun, T., Neuberg, J., Ripepe, M., 1996. On the origin of the long-period tremor recorded at Stromboli volcano (Italy). Ann. Geofis. 39, 311–326.

Canas, J.A., Ugalde, A., Pujades, L.G., Carracedo, J.C., Soler, V., Blanco, M.J., 1998. Intrinsic scattering and seismic wave attenuation in the Canary Islands. J. Geophys. Res. 103, 15 037–15 050.

Capon, J., 1969. High-resolution frequency-wavenumber spectrum analysis. Proc. IEEE 57, 1408–1418.

Chouet, B.A., 1996. Long-period volcano seismicity: its source and use in eruption forecasting. Nature 380, 309–316.

Chouet, B.A., Saccorotti, G., Martini, M., Dawson, P., De Luca, G., Milana, G., Scarpa, R., 1997. Source and path effects in the wave fields of tremor and explosions at Stromboli Volcano, Italy. J. Geophys. Res. 102, 15129–15150.

Del Pezzo, E., La Rocca, M., Ibanez, J.M., 1997. Observations of high-frequency scattered waves using dense arrays at Teide volcano. Bull. Seismol. Soc. Am. 87, 1637–1647.

Del Pezzo, E., La Rocca, M., Petrosino, S., Grozea, B., Maritato, L., Saccorotti, G., Simini, M., Ibáñez, J.M., Alguacil, G., Carmona, E., Abril, M., Almendros, J., Ortiz, R., García, A., Pingüe, F., Esposito, T., 1998. Twin digital short period seismic array experiment at Stromboli Volcanol. Open-file report, Osservatorio Vesuviano.

Ferrazzini, V., Aki, K., Chouet, B.A., 1991. Characteristics of seismic waves composing hawaiian volcanic tremor and gas-piston events observed by a near-source array. J. Geophys. Res. 96, 6199–6209.

Filmer, P., McNutt, M., 1989. Geoid anomalies over the Canary Islands Group. Mar. Geophys. Res. 11, 77–87.

Frankel, A., Hough, S., Friberg, P., Busby, R., 1991. Observations of Loma Prieta aftershocks from a dense array in Sunnyvale, California. Bull. Seism. Soc. Am. 81, 1900–1922.

Goldstein, P., Chouet, B.A., 1994. Array measurements and modeling of sources of shallow volcanic tremor at Kilauea Volcano, Hawaii. J. Geophys. Res. 99, 2637–2652.

Ibáñez, J.M., Morales, J., Alguacil, G., Almendros, J., Ortiz, R., Del Pezzo, E., 1997. Intermediate-focus earthquakes under South Shetland Islands (Antarctica). Geophys. Res. Lett. 24, 531–534.

LaCoss, R.T., Kelly, E.J., Toksoz, M.N., 1969. Estimation of seismic noise structure using arrays. Geophysics 34, 21–38.

Martí, J., Mitjavila, J., Araña, V., 1994. Stratigraphy, structure and geochronology of the Cañadas caldera. Geol. Mag. 131, 715–727.

Martí, J., Mitjavila, J., Araña, V., 1995. The Cañadas edifice and caldera. In: Martí, J., Mitjavila, J. (Eds.), A Field Guide to the Central Volcanic Complex of Tenerife (Canary Islands). Serie Casa de los Volcanes, vol. 4. Servicio de Publicaciones del Cabildo Insular de Lanzarote, pp. 19–38.

Métaxian, J.P., Lesage, P., Dorel, J., 1997. Permanent tremor of Masaya volcano, Nicaragua: wave field analysis and source location. J. Geophys. Res. 102, 22529–22545.

Mezcua, J., Galán, J., Rueda, J.J., Martínez, J., Buforn, E., 1990. Sismotectónica de las islas Canarias. Estudio del terremoto del 9 de Mayo de 1989 y su serie de réplicas. Publ. Técnica, 23, IGN, Madrid.

Mezcua, J., Buforn, E., Udías, A., Rueda, J., 1992. Seismotectonics of the Canary Islands. Tectonophysics 208, 447–452.

Ortiz, R., Araña, V., Astiz, M., García, A., 1986. Magnetotelluric study of the Teide (Tenerife) and Timanfaya (Lanzarote) volcanic areas. J. Volcanol. Geotherm. Res. 30, 357–377.

Saccorotti, G., 1997. Studio del campo d'onda sismico a corto periodo associato all'attività vulcanica dello Stromboli (in Italian). Tesi di dottorato, Univ. degli Studi di Napoli.

Scarpa, R., Patanè, G., Lombardo, G., 1983. Space–time evolution of seismic activity at Mount Etna during 1974–1982. Ann. Geophys. 6, 451–462.

Schmidt, R.O., 1986. Multiple emitter location and signal parameter estimation. IEEE Trans. Ant. Prop. 34, 276–280.

Sevilla, M., Romero, P., 1991. Ground deformation control by statistical analysis of a geodetic network in the caldera of Teide. J. Volcanol. Geotherm. Res. 47, 65–74.

Spudich, P., Bostwick, T., 1987. Studies of the seismic coda using an earthquake cluster as a deeply buried seismograph array. J. Geophys. Res. 92, 10526–10546.

Valentín, A., Albert-Beltrán, J.F., Díez, J.L., 1990. Geochemical and geothermal constraints on magma bodies associated with historic activity, Tenerife (Canary Islands). J. Volcanol. Geotherm. Res. 44, 251–264.

Watts, A.B., 1994. Crustal structure, gravity anomalies and flexure of the litosphere in the vicinity of the Canary Islands. Geophys. J. Int. 119, 648–666.